CivilEng

MDPI

*Article*

# Multi-Objective Optimization and Road Texture Detection Based on an Interdigitated Coplanar Array Capacitance Sensor

**Jiejia Guo [1], Bin Shi [2] and Zhen Liu [3,*]**

[1] Hunan Provincial Communications Planning, Survey & Design Institute Co., Ltd., Changsha 410200, China
[2] Civil Engineering Department, Hefei University of Technology, Hefei 230009, China; binshi@hfut.edu.cn
[3] Institute of Space and Earth Information Science, The Chinese University of Hong Kong, Hong Kong 999077, China
* Correspondence: zhenliu@cuhk.edu.hk

## Abstract

Coplanar capacitance detection exhibits remarkable advantages in the detection of road texture in asphalt layers, including high sensitivity and minimal environmental constraints. However, the inherent performance contradiction between signal strength and penetration depth of traditional interdigitated coplanar capacitance sensors (ICCSs) has restricted their widespread application in road texture detection. To address this issue, a hybrid approach combining response surface methodology (RSM) and non-dominated sorting genetic algorithm II (NSGA-II) is developed to optimize the structural parameters that influence the signal strength and penetration depth of a novel ICCS. Initially, a central-composite design (CCD) based on RSM is employed to establish statistical models for the two key sensing performances of ICCSs, namely signal strength and penetration depth. Subsequently, Analysis of Variance (ANOVA) and three-dimensional (3D) response surface plots are utilized to investigate the significant effects of various structural parameters (electrode length, width, and inter-finger gap) on the two sensing performances. Furthermore, NSGA-II is applied to search for global optimal solutions using the established statistical models, thereby achieving multi-performance optimization of the ICCS. Finally, the fabricated ICCS is used to detect the surface texture of asphalt mixture specimens with different gradations, and the results are compared with those obtained by laser point cloud detection. The results indicate that both statistical models are highly significant, with the coefficient of determination (R-squared) exceeding 0.95. All individual structural parameters have a significant impact on the two sensing performances. Based on the optimization by the RSM-NSGA-II hybrid method, the predicted optimal parameters are verified, showing a relative error of less than 5% from the simulation results. Additionally, the detection results of the ICCS are consistent with the laser point-cloud data, demonstrating its feasibility for pavement texture detection.

**Keywords:** road texture detection; interdigitated coplanar array capacitance sensors; response surface methodology; multi-objective optimization; surface texture reconstruction

Check for updates

Academic Editors: Angelo Luongo, Saman Hedjazi and Hossein Taheri

Received: 1 June 2026
Revised: 24 July 2026
Accepted: 28 July 2026
Published: 30 July 2026

**Copyright:** © 2026 by the authors. Licensee MDPI, Basel, Switzerland. This article is an open access article distributed under the terms and conditions of the Creative Commons Attribution (CC BY) license.

## 1. Introduction

Road surface texture is one of the key factors affecting the skid resistance of highways, significantly influencing vehicle handling stability and driving safety. Surface texture primarily consists of macro-texture and micro-texture, and the characteristics of these textures directly affect the contact mode between tires and the road surface, thus impacting

vehicle braking distance and surface skid resistance [1–3]. Additionally, road surface texture is closely related to pavement drainage performance, the contact area between tires and the road, and driving comfort [4,5]. Especially in rainy, snowy weather and during high-speed driving, the skid resistance of the road surface directly determines vehicle safety and the likelihood of traffic accidents [6–8]. Expressway interchanges, especially speed-change lane segments, witness frequent pavement damage and traffic accidents. Pavement texture detection in these areas demands a higher precision level than that for ordinary mainline road sections.

The sand patch method, as an artificial measurement technique, offers low cost and ease of operation. However, it relies heavily on the proficiency of the engineers, leading to lower accuracy in measured results [9,10]. The mechanical profilometer can capture road surface texture with high resolution, but it presents complexities in equipment calibration and reduced precision on surfaces with significant rutting or undulation [11,12]. A road surface detection vehicle can obtain high accuracy in texture detection while on the move, but it is expensive and requires high maintenance costs [13,14]. Laser detection, as a non-contact detection method, provides excellent speed and precision; however, it is sensitive to environmental noise such as dust and water droplets, and the vast amounts of point cloud data can pose significant data storage challenges [15–17]. Image-based detection methods possess the merits of low cost, convenient operation and abundant spatial data information, while they suffer from environmental interference, empirical algorithm parameters, poor repeatability and insufficient micro-texture detection accuracy [15–18].

Coplanar capacitance sensing technology measures properties such as distance, thickness, and texture of target objects through variations in the dielectric constant between interdigitated coplanar capacitance sensor electrodes [19–21]. It offers a high sensitivity to minute dielectric changes and does not require direct contact [22,23]. Moreover, it shows high tolerance to environmental noise from dust and water droplets, allowing stable detection across various environments [24,25]. The interdigitated coplanar capacitance sensing technology has already found mature applications in fields such as biochemical detection, environmental monitoring, and industrial process control, thus presenting great potential for its application in road surface texture detection [26–28].

Interdigital capacitance sensors mainly include equidistant-parallel interdigital type, variable-pitch interdigital type, annular interdigital type, and interleaved-complementary interdigital type. The equidistant-parallel interdigital type has uniform electrode finger width and spacing, with a regular electric field distribution, but it has the disadvantage of limited detection sensitivity [29,30]. The variable-pitch interdigital type can adapt to detection targets of different depths and thicknesses through the gradient change of electrode finger spacing. However, its electric field distribution is complex, leading to great difficulty in signal analysis [31,32]. The annular interdigital type has electrodes arranged in a ring shape, with the electric field distributed radially. It is suitable for the directional detection of local point features and micro-particle morphology, but it has a limited detection range [33,34]. The interleaved complementary interdigital type achieves high detection sensitivity through the interleaved and nested arrangement of positive and negative electrodes. It is applicable to the accurate identification of micro-scale mesoscopic features, yet its structure is complex and it is prone to interference from external electromagnetic fields [35].

This investigation adopts equal-width and equal-spacing parallel interdigital coplanar capacitance sensors (ICCSs) to detect road surface texture. Given the differences in the distribution, morphology, and geometric dimensions of surface textures within asphalt pavement layers, ICCSs are required to possess favorable signal response strength. Meanwhile, in view of the depth-dependent characteristics of pavement surface textures, such

sensors are demanded to achieve a relatively large effective penetration depth ranging from 3 mm to 4 mm. Nevertheless, there exists an inherent contradiction between signal strength and penetration depth in the parameter optimization of ICCSs. Consequently, targeted structural optimization and customized design for such sensors are essential to balance sufficient signal strength and ideal penetration depth, thereby acquiring superior texture detection performance. Equipped with high precision for road texture quantification, the optimized sensor facilitates the evaluation of pavement anti-skid performance and guides targeted pavement maintenance, thereby providing a technical guarantee for road traffic safety.

Recently, a few ICCSs have been used to identify road surface texture. Therefore, this study aims to develop and optimize an ICCS for detecting road surface texture based on this method (response surface methodology (RSM) with central-composite design (CCD) + non-dominated sorting genetic algorithm II (NSGA-II) optimization). The contributions of this study in the multi-objective optimization of ICCSs are structured into four main parts: (a) establishing a statistical model of RSM-CCD to determine the predicted equation of sensor performances; (b) analyzing the effect of sensor parameters on the signal strength and penetration depth; (c) determining the optimal sensor structure through multi-objective optimization analysis of NSGA-II; and (d) reconstructing road surface texture using point cloud detection and coplanar capacitance detection.

## 2. Sensor Design and Optimization

### 2.1. Road Texture Detection Theory Based on ICCSs

Interdigital coplanar capacitance detection acquires road texture distribution based on the permittivity differences caused by the varying medium distribution of asphalt mixtures on road surfaces. As shown in Figure 1, the ICCS can accurately measure the permittivity distribution of the measured object [36]. Nevertheless, the spatial distribution of electric field lines of the sensor is non-uniform, and external environmental factors also exert certain influences on coplanar capacitance measurement. When the ICCS starts to identify the distribution of the measured object, the distribution of electric field lines in the steady-state electric field alters, accompanied by changes in permittivity such as capacitance values [37]. Accordingly, the permittivity distribution within asphalt mixtures can be derived from capacitance discrepancies across distinct electrode pairs, enabling the reconstruction of road texture.

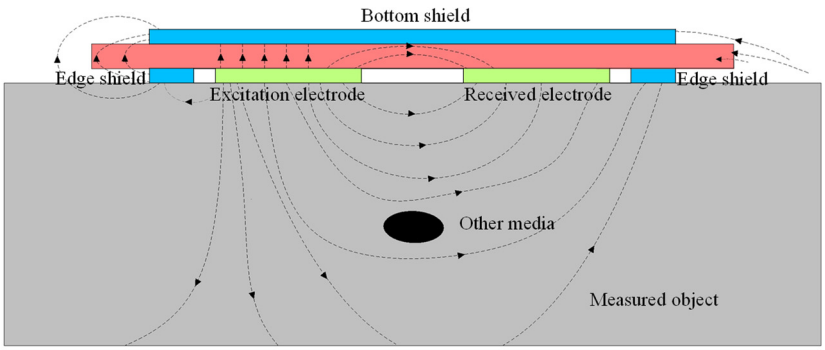


**Figure 1.** The detection theory of the ICCS.

### 2.2. Structure and FEM Construction of the ICCS

The core components of the ICCS designed in this study include four parallel metal electrodes and an insulating substrate, as shown in Figure 2. The four electrodes are arranged alternately to form an interdigitated structure, with each electrode sized at L (length) × W (width). A gap with a width of G is left between adjacent electrodes, result-

ing in a center-to-center distance of W + G between two adjacent electrodes. The electrodes are positioned on the surface of the substrate, which is made from a material with a stable dielectric constant and low dielectric loss, such as epoxy glass fiber or polytetrafluoroethylene. The substrate serves to support the electrodes and achieve electrical isolation.

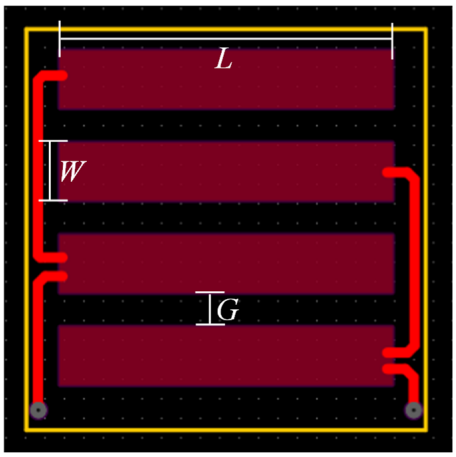


**Figure 2.** Dimensional design of the ICCS.

COMSOL Multiphysics version 5.5 is utilized for finite element modeling (FEM) and simulation of the ICCS, as depicted in Figure 3. The related parameters of the ICCS are listed in Table 1. A voltage of 5 V is applied to the excitation electrode, while the other electrodes are sequentially grounded, thereby forming an electrostatic field beneath the plates of the sensor. The geometric domain primarily includes the interdigital electrodes made of copper, the dielectric medium set with air, and the test object set with asphalt mixture. For mesh settings, a coarser mesh is applied to the air domain, while a refined mesh is used for other sections, ensuring the accuracy of calculations for parameters such as surface charge density and capacitance values.

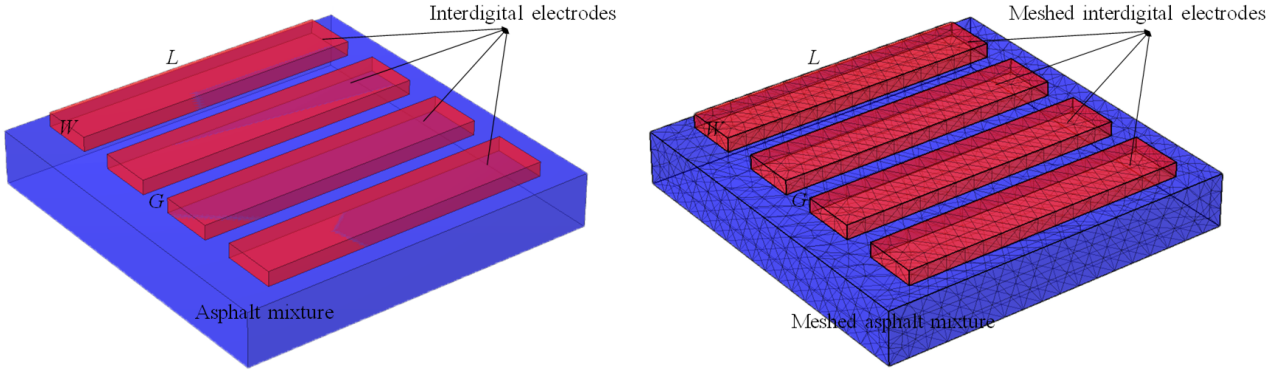


(**a**) Modeling of ICCS (**b**) Meshing of ICCS

**Figure 3.** FEM of the ICCS.

**Table 1.** Related parameters of the ICCS model.

| Parameters | Units | Values |
|---|---|---|
| Electrode size | mm | $L \times W$ |
| Inter-finger gap | mm | $G$ |
| Electrode number | / | 4 |
| Substrate thickness | mm | $H$ |
| Excitation voltage | V | 5 |

### 2.3. Structural Parameters and Optimized Objects

The performance of the ICCS mainly includes penetration depth and signal strength. The penetration depth characterizes the effective action range of the electric field of the sensor in the dielectric medium, while the signal strength directly determines the detection sensitivity. Signal strength serves as a crucial indicator in sensor design. A higher signal strength can improve the signal-to-noise ratio (SNR) and render experimental results more prominent [38]. In contrast, a lower signal strength enables more stable sensor detection, endowing the sensor with favorable robustness and stable detection capability. The signal strength is represented by the capacitance value $C^*$ between electrode pairs. Penetration depth is a key performance indicator of coplanar capacitance sensors. Taking 3% of the dynamic range as the threshold (defined as the difference between the capacitance at z = 0 and the capacitance approaching z = ∞), γ3% is defined as the effective penetration depth [39]. The effective penetration depth (H) is calculated according to the following formula:

$$\frac{C(z=\gamma_{3\%}) - C(z\to\infty) \times 100\%}{C(z=0) - C(z\to\infty)} = 3\% \quad (1)$$

where $C(z=\gamma_{3\%})$ is the capacitance at the 3% effective measuring distance in picofarads, pF; $C(z=0)$ denotes the capacitance when the distance between the sensor and the surface of the measured object is zero, pF; and $C(z\to\infty)$ represents the capacitance at an infinite distance between the sensor and the measured object surface, pF.

The electrode length (L), electrode width (W), and inter-finger gap (G) of interdigital electrodes all exert significant influences on the electric field distribution. Increasing the electrode length can extend the longitudinal propagation path of the electric field along the electrode, which is conducive to expanding the detection area. However, excessively long electrodes may introduce noise induced by edge effects. Increasing the electrode width can raise the charge density per unit area, thereby enhancing the signal strength in the near-field region, while narrowing the coverage range of the effective electric field. The variation of the inter-finger gap directly determines the lateral diffusion and longitudinal penetration characteristics of the electric field within the dielectric medium. Accordingly, this study takes penetration depth and signal strength as the optimized objects and regards electrode length, electrode width, and inter-finger gap as the structural optimization variables of the sensor.

### 2.4. Statistical Balanced Sensor Design

In this study, RSM coupled with CCD is employed to optimize the structural parameters of the ICCS. As one of the most prominent experimental design methods in RSM, CCD is adopted for computational analysis via Design-Expert software (version 13). Meanwhile, the RSM-CCD approach is utilized to determine the optimal response input factors. The electrode length, the electrode width, and inter-finger gap are selected as the input variables. The selection of experimental data points covered all design points at the +1 and −1 levels, a designated central point, as well as axial points at the $-\alpha$ and $+\alpha$ levels. Herein, α (alpha) is the axial distance scaling parameter of the central composite design, which governs the distance from the design center point to the axial star points and expands the experimental range beyond the factorial level of ±1 to facilitate quadratic response surface fitting. The input factors, their corresponding code, and levels are described in Table 2 (α = 2 for three factors).

The equations for the two optimization indicators of the sensor (signal strength and penetration depth) are generally estimated using a quadratic model and expressed in the form of a second-order polynomial, as follows:

$$y = \beta_0 + \sum_{i=1}^{n} \beta_i x_i + \sum_{i=1}^{n} \beta_{ii} {x_i}^2 + \sum_{i=1}^{n} \sum_{j>1}^{n} \beta_{ij} x_i x_j \quad (2)$$

where $y$ denotes the output responses; and $\beta_0$, $\beta_i$, $\beta_{ii}$ and $\beta_{ij}$ represent the unknown regression coefficients estimated via least squares regression. Specifically, $\beta_0$ is the constant term, while $\beta_0$, $\beta_i$, $\beta_{ii}$ and $\beta_{ij}$ correspond to the linear, quadratic and interaction coefficients, respectively; $x_i$, $x_j$ are the coded values of the input factors that govern the output responses. As listed in Table 3, fifteen experimental runs are randomly selected in accordance with the three-factor CCD arrangement incorporating central points.

**Table 2.** Boundaries of input factors in RSM-CCD.

| Factor | Code | Level | | | | |
|---|---|---|---|---|---|---|
| | | $-\alpha$ | −1 | 0 | 1 | $+\alpha$ |
| $L$ (mm) | A | 2 | 4 | 6 | 8 | 10 |
| $W$ (mm) | B | 0.9 | 1.2 | 1.5 | 1.8 | 2.1 |
| $G$ (mm) | C | 0.6 | 0.7 | 0.8 | 0.9 | 1.0 |

**Table 3.** RSM-CCD detail of sensor configuration.

| Runs | Coded Values | | | Mass | | |
|---|---|---|---|---|---|---|
| | A | B | C | $L$ (mm) | $W$ (mm) | $G$ (mm) |
| S1 | −1 | −1 | 1 | 4 | 1.2 | 0.9 |
| S2 | 0 | 0 | 2 | 6 | 1.5 | 1.0 |
| S3 | 2 | 0 | 0 | 10 | 1.5 | 0.8 |
| S4 | 1 | −1 | 1 | 8 | 1.2 | 0.9 |
| S5 | 0 | 0 | −2 | 6 | 1.5 | 0.6 |
| S6 | −2 | 0 | 0 | 2 | 1.5 | 0.8 |
| S7 | 0 | 2 | 0 | 6 | 2.1 | 0.8 |
| S8 | 0 | 0 | 0 | 6 | 1.5 | 0.8 |
| S9 | 1 | 1 | −1 | 8 | 1.8 | 0.7 |
| S10 | −1 | −1 | −1 | 4 | 1.2 | 0.7 |
| S11 | −1 | 1 | 1 | 4 | 1.8 | 0.9 |
| S12 | 1 | 1 | 1 | 8 | 1.8 | 0.9 |
| S13 | 0 | −2 | 0 | 6 | 0.9 | 0.8 |
| S14 | −1 | 1 | −1 | 4 | 1.8 | 0.7 |
| S15 | 1 | −1 | −1 | 8 | 1.2 | 0.7 |

### *2.5. Multi-Objective Optimization Method*

NSGA-II (non-dominated sorting genetic algorithm II) is a classical multi-objective optimization method, which exhibits remarkable theoretical and practical advantages in addressing engineering problems with conflicting objectives [36,40,41]. In this study, finite element simulation is combined with NSGA-II to collaboratively optimize the structural parameters of the ICCS [41–43]. The main implementation procedures of NSGA-II are presented as follows:

1. Population initialization. Each individual in the initial population is generated randomly by uniform random numbers.
2. Placement of reference points on the hyperplane. A set of predefined reference points is adopted to maintain the diversity of individuals.
3. Selection of parent population. Tournament comparison based on the non-dominated sorting algorithm is employed to select parents and offspring from the parent population.
4. Crossover and mutation. Simulated binary crossover and polynomial mutation are applied to the parental individuals to generate the offspring population.
5. Adaptive normalization of objective functions. Normalization is used to associate the combined population with reference points and unify their value ranges.
6. Reference-point-based selection. The normalized objective values are correlated with the reference points to complete population member selection.

## 3. Road Surface Texture Detection

### *3.1. Sample Preparation*

The texture depth and surface texture of asphalt pavement vary significantly, mainly due to differences in asphalt mixture types. Therefore, three gradation types are prepared for further detection, including dense-graded asphalt concrete (AC-10), stone matrix asphalt (SMA-10), and open-graded friction course (OGFC-10), as depicted in Figure 4. Basalt aggregate and penetration grade-virgin 70 asphalt are selected as raw materials for specimen preparation. All specimens are fabricated in accordance with the rutting slab preparation method specified in the Standard Test Methods of Bitumen and Bituminous Mixtures for Highway Engineering (JTG E20-2011) [44], with dimensions of 300 mm × 300 mm × 50 mm.

(**a**) AC-10 (**b**) OGFC-10 (**c**) SMA-10

**Figure 4.** Asphalt mixture sample.

### *3.2. Laser Scanning Detection*

The Leica AT960 absolute laser scanning system is adopted to perform three-dimensional coordinates of pavement surfaces (Leica Geosystems AG, Heerbrugg, Switzerland). As depicted in Figure 5, the scanning process adopted six-degree-of-freedom calibration consisting of a laser transmitter (LAT) and a mobile sensor (LAS). A thermal expansion coefficient compensation module is used to eliminate the datum drift error induced by ambient temperature fluctuations. During data acquisition, the mobile sensor moves along a predefined trajectory at a constant speed of 0.15 m/s, and the triggering sampling frequency is dynamically adjusted within the range of 200–500 Hz according to the surface curvature. To ensure data integrity, the system is equipped with a built-in real-time point cloud coverage analysis module, which automatically activates a secondary rescanning procedure for shadowed areas. The areal point density of a single scan is strictly controlled at 1 mm per point. Pre-experimental verification demonstrated that the system can stably capture surface depressions as small as 0.2 mm.

(**a**) A mobile sensor (**b**) Laser scanning detection

**Figure 5.** Laser scanning detection process.

### *3.3. Coplanar Capacitance Scanning Detection*

To verify the sensing performance of the ICCS with optimized configuration, the corresponding sensor prototypes and PCB boards are fabricated, and the matched control chip is employed to realize Bluetooth data transmission. As shown in Figure 6a, four sensors are arranged on the PCB board. The structural configuration of the sensor is described as follows: the sensor consists of four electrodes in total. As depicted in Figure 6b, the control chip adopted is the PCAP02, which has a total of 16 pins. Among them, the eight left pins are assigned to GND. Two pairs of sensors (two sets of red and black wires in total) are connected to the right pins, and two such control chips are used for connection and testing. The PCB board fabricated for the sensor has dimensions of 2.5 cm × 2.5 cm. A total of 144 measurements is required to cover the 30 cm × 30 cm specimen. It acquires 900 sampling points in total.

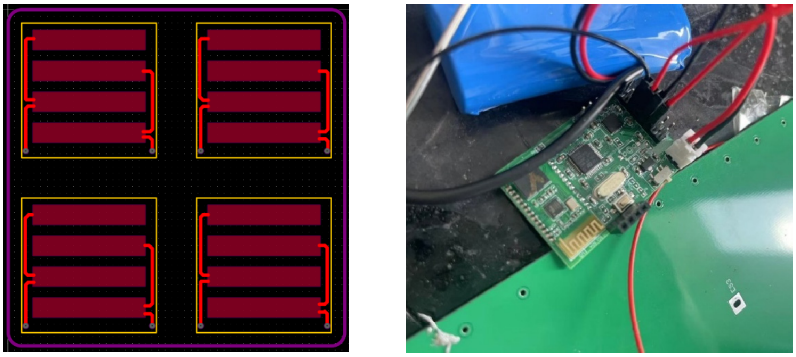

(**a**) PCB with ICCSs (**b**) Assembly of PCB and measurement chips

**Figure 6.** Assembly of the capacitance detection device.

The ICCS measurements are repeated three times, yielding a relative standard deviation below 1.2%, while laser measurements are performed in six parallel groups with a maximum repeatability error of ±0.03 mm. Pre-experiment zero calibration is implemented to eliminate sensor positioning errors. All tests were conducted in a constant-temperature and constant-humidity environment, which effectively suppressed environmental measurement uncertainties and guaranteed the validity and reliability of the experimental results.

## 4. Results and Discussion

### *4.1. Development of Statistical Models*

The simulation results derived from the RSM-CCD design, including signal strength and penetration depth, are summarized in Table 4. The signal strength ranges from 0.212 to 0.356, while the penetration depth varies between 2.29 mm and 4.10 mm. To further verify the applicability of the established mathematical models, statistical validation is performed using Design-Expert 13 software. The ANOVA outcomes for the regression models of signal strength ($C^*$) and penetration depth (H) are presented in Table 5.

**Table 4.** Simulation results obtained from RSM-CCD.

| Runs | Signal Strength ($C^*$) | Penetration Depth ($H$/mm) | Runs | Signal Strength ($C^*$) | Penetration Depth ($H$/mm) |
|---|---|---|---|---|---|
| S1 | 0.224 | 2.71 | S9 | 0.341 | 2.86 |
| S2 | 0.276 | 2.98 | S10 | 0.235 | 2.90 |
| S3 | 0.356 | 3.40 | S11 | 0.243 | 2.76 |
| S4 | 0.299 | 2.94 | S12 | 0.335 | 3.16 |
| S5 | 0.323 | 4.10 | S13 | 0.258 | 3.20 |
| S6 | 0.212 | 2.99 | S14 | 0.279 | 2.29 |
| S7 | 0.323 | 3.00 | S15 | 0.312 | 2.78 |
| S8 | 0.279 | 2.86 | | | |

**Table 5.** ANOVA for the regression model and respective model terms.

| Source | Signal Strength | | | | Penetration Depth | | | |
|---|---|---|---|---|---|---|---|---|
| | **MS.** | **F-Value** | ***p*-Value** | **Sig.** | **MS.** | **F-Value** | ***p*-Value** | **Sig.** |
| Model | 0.0032 | 54.59 | <0.0001 | Y | 0.0052 | 3.35 | 0.0366 | Y |
| A | 0.0221 | 381.69 | <0.0001 | Y | 0.0066 | 4.29 | 0.0651 | Y |
| B | 0.0041 | 71.38 | <0.0001 | Y | 0.0008 | 5.89 | 0.0350 | Y |
| C | 0.0016 | 27.32 | 0.0004 | Y | 0.0085 | 5.51 | 0.0408 | Y |
| A × B | $6.50 \times 10^{-7}$ | 0.0112 | 0.9176 | N | 0.0013 | 0.8167 | 0.3874 | N |
| A × C | 0.0001 | 1.77 | 0.2124 | N | 0.0003 | 0.1962 | 0.6672 | N |
| B × C | 0.0 | 0.07451 | 0.4083 | N | 0.0081 | 5.28 | 0.0443 | Y |
| $A^2$ | $3.10 \times 10^{-8}$ | 0.0005 | 0.9820 | N | 0.0015 | 1.00 | 0.3399 | N |
| $B^2$ | 0.0001 | 1.28 | 0.2848 | N | 0.0183 | 11.90 | 0.0062 | Y |
| $C^2$ | 0.0004 | 7.58 | 0.0204 | Y | 0.0034 | 2.24 | 0.1657 | N |
| Residual | 0.0001 | - | - | - | 0.0015 | - | - | - |
| R-squared | 0.9561 | | | | 0.9781 | | | |

Note: MS.—mean squares; Sig.—significant; Y—yes; N—no.

In general, model terms with a *p*-value below 0.05 are statistically significant, whereas those with a *p*-value exceeding 0.05 are considered insignificant. As presented in Table 5, the model terms for both signal strength and penetration depth yield a *p*-value of less than 0.0001, confirming the statistical significance of the two regression models. Additionally, the high coefficients of determination ($R^2$ = 0.9561 and 0.9781) demonstrate that the established regression models are well suited for predictive analysis.

A significance test for the input factors is performed at the 5% significance level. Based on regression coefficient estimates, the following quadratic regression equations are established to correlate the three factors (A-L, B-W and C-G) and further predict signal strength ($C^*$) and penetration depth (H).

Signal strength ($C^*$):

$$C^* = 0.2793 + 0.0402 * A + 0.0174 * B - 0.0108 * C + 0.0003 * A * B + 0.0036 * A * C + 0.023 * B * C + 0 * A^2 + 0.0023 * B^2 + 0.0055 * C^2 \quad (3)$$

Penetration depth ($H$):

$$H = 2.88 + 0.1296 * A - 0.0437 * B - 0.0837 * C + 0.1075 * A * B + 0.0225 * A * C + 0.1 * B * C + 0.0121 * A^2 - 0.0214 * B^2 + 0.1341 * C^2 \quad (4)$$

### *4.2. Effect of Structural Parameters on Sensing Performance*

The *p*-values (<0.0001) of signal strength and penetration depth in Table 5 demonstrate that the established regression models possess high statistical significance. Among the three structural parameters affecting signal strength, parameters A and B exert the most prominent influence, followed by parameter C. This indicates that the electrode length and electrode width are the primary factors determining the signal strength of the ICCS, with the inter-finger gap being the secondary factor. In terms of penetration depth, the ANOVA *p*-values confirm the statistical significance of the corresponding model, which can be reliably adopted to predict the penetration depth. Parameter C (inter-finger gap) and parameter A (electrode length) dominate the influence on penetration depth, followed by parameter B (electrode width). The interaction term B × C exhibits a significant effect on penetration depth.

The effects of sensor geometric configurations, namely electrode length, electrode width and inter-electrode spacing, on the overall sensing performance can be intuitively visualized through three-dimensional (3D) response surface diagrams. The color gradient

in the 3D response surface plots reflects the magnitude of the effect of each factor on the response values. Specifically, the red region corresponds to a steep response surface slope, indicating a significant influence of the corresponding factor on the response. In contrast, the blue region represents a gentle slope of the response surface, suggesting an insignificant effect of the factor on the response. The gradual color transition from blue to red implies an increase in the steepness of the response surface slope, which accelerates the variation of the response and enhances the impact of the corresponding factor.

Figure 7 presents the three-dimensional response surface plots of the interaction terms A × B, A × C, and B × C for signal strength. For a fixed electrode width, the signal strength increases markedly with the rise in electrode length, indicating that the signal strength of the ICCS increases as the electrode length increases. As the electrode length is fixed and the inter-electrode gap is reduced, the increase in $C^*$ is significant. This reveals that the inter-electrode gap exerts a remarkable negative effect on the signal strength of the sensor. In addition, increasing the electrode width under a fixed electrode length enhances the measured coplanar capacitance, demonstrating that electrode width is also a critical factor affecting the signal strength of the sensor.

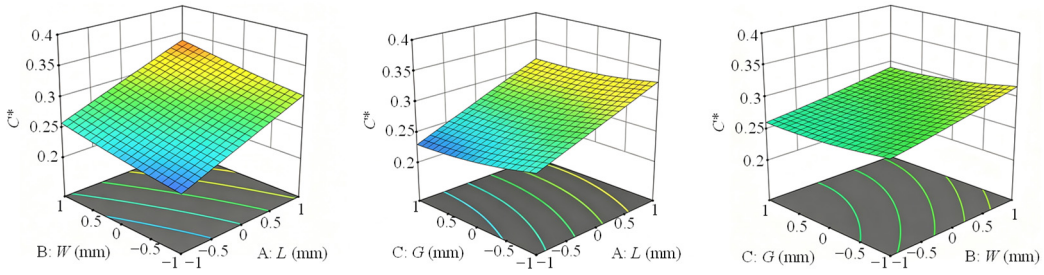


(**a**) (**b**) (**c**)

**Figure 7.** 3D response surface plots of $C^*$: (**a**) A × B; (**b**) A × C; (**c**) B × C.

Figure 8 displays the 3D response surface plots of interaction terms A × B, A × C, and B × C for penetration depth. The penetration depth rises sharply with the increase in electrode length, indicating that a longer electrode contributes to a greater penetration depth of the ICCS. Meanwhile, the penetration depth increases correspondingly as electrode width rises, suggesting that a larger electrode width can also improve the penetration depth, though such an effect is evidently less pronounced than that of the electrode length. A smaller value of inter-electrode gap yields a larger penetration depth, which demonstrates that the inter-electrode gap exerts a significant negative influence on penetration depth; that is, the penetration depth increases as the inter-electrode gap decreases. Overall, a larger electrode length combined with a smaller inter-electrode gap can substantially enhance the penetration depth. Accordingly, the penetration depth can be effectively improved by increasing the electrode length while reducing the inter-electrode gap simultaneously.

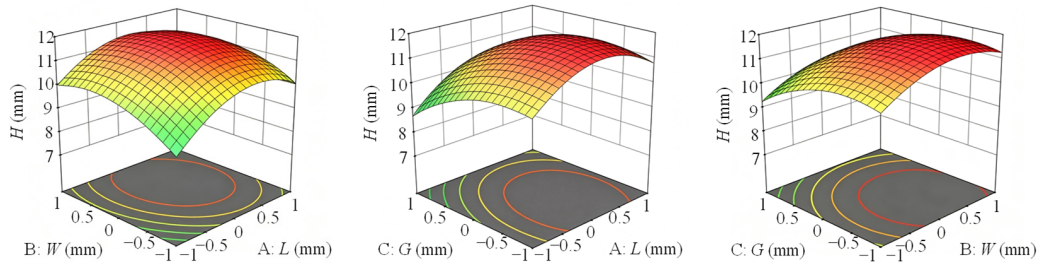


(**a**) (**b**) (**c**)

**Figure 8.** 3D response surface plots of $H$: (**a**) A × B; (**b**) A × C; (**c**) B × C.

### 4.3. Multi-Objective Optimization Analysis

For ICCSs with identical electrode number and geometric morphology, signal strength and penetration depth are primarily determined by three structural parameters: electrode length, electrode width, and inter-finger gap. As aforementioned, a trade-off relationship exists between signal strength and penetration depth, such that the two performance indicators cannot reach their individual optimal values simultaneously. Accordingly, this work targets the synchronous maximization of signal strength and penetration depth. The quadratic polynomial regression models established based on response surface methodology coupled with central composite design (RSM-CCD), as presented in Equations (3) and (4), are employed as fitness functions to search for the global optimal solution. Key parameter configurations and constraint conditions of NSGA-II are listed in Table 6, in which the decision variables A, B and C are assigned coded values within the range of −2 to 2.

**Table 6.** Parameters and constraint conditions of NSGA-II.

| Parameters | Value | Constraint Conditions | Range |
|---|---|---|---|
| Population size | 200 | $C^*$ (weight = 0.4) | >0.25 |
| Maximum iteration | 500 | $H$ (weight = 0.2) | >2 mm |
| Crossover probability | 0.75 | | |
| Mutation rate | 0.10 | | |

NSGA-II is implemented via the Geatpy library in Python 3.4.2, and the corresponding pseudocode is compiled to perform the structural optimization of the ICCS. Following 500 evolutionary generations, 100 Pareto optimal solutions are generated in the decision variable space. In accordance with the technical design criteria of the ICCS, the signal strength is constrained to be no less than 0.25, while the penetration depth is required to exceed 2 mm. These performance thresholds are formulated as the constraint conditions for the NSGA-II optimization process. The Pareto optimal solution set is further evaluated using a simplified multi-attribute decision-making method. A comprehensive evaluation score ranging from 0 to 1 is calculated via this approach. A higher score implies that the corresponding structural parameter combination of the ICCS better conforms to the design decision preferences. Accordingly, the optimal structural parameters of the ICCS can be finalized by ranking and filtering the non-dominated solutions according to their comprehensive scores.

The weighting coefficients of signal strength and penetration depth are set to 0.4 and 0.6, respectively. The optimized structural parameters and performance indicators of the ICCS are presented in Table 7. The coded design variables of the optimal solution determined are A = 2.004, B = 0.000, and C = 0.0375, corresponding to an electrode length (L = 10.02 mm), electrode width (W = 1.50 mm), and inter-finger gap (G = 0.83 mm). The optimally configured ICCS achieves an improved signal strength while fully satisfying the penetration depth requirement. Three groups of physical prototype experiments are carried out to verify the optimized ICCS performance. Multiple repeated measurements are performed for each experimental condition to reduce accidental errors. Notably, the dataset for establishing the RSM optimization model is acquired from finite element simulation, while the physical tests are utilized to validate the feasibility and accuracy of the optimized sensor structural parameters. Further determination of the actual signal strength and penetration depth is achieved through physical testing of a prototyped interdigital coplanar capacitance sensor bearing identical optimized geometric parameters The actual signal strength and penetration depth are 0.422 and 3.553 mm, respectively. The relative error between the actual and predicted values is less than 5%, which verifies the high robustness and credibility of the NSGA-II optimization predictions.

**Table 7.** Optimized structural parameters and objects of the ICCS.

| Structural Parameters | | | | Optimized Objects | | |
|---|---|---|---|---|---|---|
| **Type** | **Electrode Length (*L*/mm)** | **Length–Width Ratio of Electrode (*W*/mm)** | **Transverse Electrode Space (*G*/mm)** | **Type** | **Signal Strength ($C^*$)** | **Penetration Depth (*H*/mm)** |
| Coded | 2.004 | 0.000 | 0.0375 | Predicted | 0.413 | 3.475 |
| Real | 10.02 | 1.50 | 0.83 | Actual | 0.422 | 3.553 |
| | | | | Error (%) | 2.18 | 2.24 |

The integrated framework combining RSM and NSGA-II for multi-objective optimization of ICCSs enables the efficient acquisition of optimal structural parameters, offering a reliable technical reference for fine characterization of road texture within asphalt pavement layers.

### *4.4. Reconstruction of Road Surface Texture*

The optimal sensor structure obtained via multi-objective optimization is adopted to fabricate sensors in accordance with Section 3.3, and road texture detection based on coplanar capacitance sensing is subsequently carried out. The ICCS adopted in this study converts the measured coplanar capacitance values into road height, while the laser point cloud data are directly acquired by a laser scanner to obtain road height information. To evaluate the feasibility of applying the ICCS to road texture detection, the road height data collected by the ICCS and the laser scanner are compared and analyzed under the same plane coordinate system. To quantitatively convert the measured coplanar capacitance values into actual pavement surface texture height, this study implemented a systematic calibration procedure. A total of 100 valid sampling points is selected, and high-precision elevation data obtained from laser point-cloud scanning is utilized as the ground truth to establish a capacitance-height prediction model via data fitting. Considering the distinct structural features and aggregate gradation differences of asphalt mixtures, independent calibration curves and corresponding prediction models are constructed for three different mixture types. This mixture-dependent calibration approach eliminates material-related measurement errors and enhances the adaptability of the coplanar capacitance detection method for various pavement structures. In addition, the dielectric stability of asphalt mixtures and its impact on calibration performance are systematically investigated. All calibration tests are conducted under constant temperature and humidity conditions with no external electrostatic interference, which maintains stable dielectric properties of asphalt mixtures and guarantees the reliability and robustness of the fitted models in laboratory environments. For practical field detection, ambient temperature and humidity only exhibit minor fluctuations during testing operations. Such subtle environmental variations barely alter the dielectric characteristics of asphalt mixtures, exerting a negligible effect on the accuracy of capacitance-height conversion and enabling the established calibration models to maintain stable and valid performance in field engineering applications.

Visual distribution images of pavement height in the plane coordinate system are generated to characterize the distribution of local road texture. In addition, mean profile depth (MPD), crest-trough height (RVD), and estimated texture depth (ETD) are adopted to quantitatively evaluate the differences between the two road texture detection methods. As shown in Figure 9a,b, the height distribution generated from point cloud data of the AC-10 specimen presents an overall uniform undulation with slight texture fluctuations in local details. By contrast, the height distribution converted from coplanar capacitance data is consistent with the characteristic of small discrete undulations of texture for AC mixtures. As described in Figure 9c,d, for the OGFC-10 specimen, the point-cloud-derived height distribution exhibits dramatic undulation variations with a large number of low-lying points in detail. The height distribution is converted from coplanar capacitance data and conforms to the feature of extremely large height differences of road texture in OGFC

mixtures. As depicted in Figure 9e,f, for the SMA-10 specimen, the height distribution generated from the laser point cloud presents an overall uniform undulation, accompanied by prominent local height variations. The height distribution converted from coplanar capacitance is consistent with the structural characteristics of SMA gradation: low overall texture dispersion but strong local particle prominence with obvious height differences.

In this study, the true texture depth values of each rut slab are acquired via the manual sand patch test to verify the reliability of the interdigitated coplanar capacitance sensing method. The mean texture depth (MTD) measured by the sand patch test is summarized in Table 8. The results reveal that the detection data obtained from the ICCS and laser scanning exhibit favorable consistency with the standard laboratory MTD measurements. Under the three different gradation types, the overall trends of pavement texture distribution detected by the coplanar capacitance method and laser point cloud are in good agreement. In addition, it can be seen from the macro-texture indicators of the three types of pavements presented in Table 8 that the difference in pavement texture detected by the coplanar capacitance method and the laser point-cloud method is negligible. The detection results of the ICCS show relatively obvious errors only in the edge region of the rut plate, while such local errors have an insignificant impact on the overall texture distribution detection. The road texture elevation data acquired by the interdigitated coplanar capacitance sensor are compared with laser point-cloud data via five statistical indicators, including the mean square error (MSE), root mean square error (RMSE), mean absolute error (MAE), coefficient of determination ($R^2$), and Pearson correlation coefficient (PCC). As illustrated in Table 9, the detection accuracy of the interdigitated coplanar capacitance sensing method is comparable to that of laser point-cloud measurement. This method performs best for OGFC asphalt mixtures, followed by SMA and AC mixtures in sequence. This indicates that the ICCS possesses satisfactory feasibility and development potential for texture detection in asphalt layers.

This paper quantitatively defines the practical applicability of the proposed interdigital coplanar capacitance sensing technique for road texture detection, covering pavement flatness tolerance, effective detection depth, and adaptable pavement gradation types. The developed sensing technology is valid for high-grade asphalt pavements with an International Roughness Index (IRI) $\leq$ 2.0 m/km and a longitudinal flatness standard deviation $\leq$ 1.2 mm. Oriented toward fine-scale evaluation of pavement surface texture, the technique achieves stable and accurate detection within the uppermost 5 mm of the pavement surface layer. In terms of engineering adaptability, the proposed method is compatible with three mainstream asphalt pavement gradations widely applied in road construction, namely AC, OGFC, and SMA.

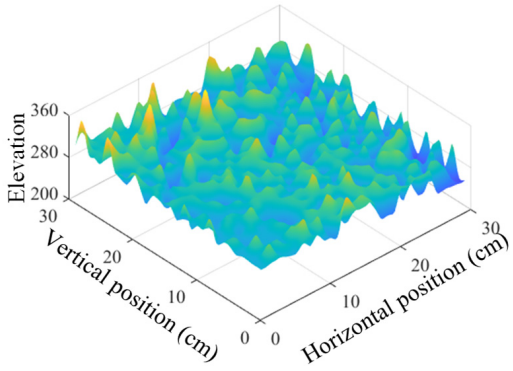


(**a**) AC-10 point cloud imaging

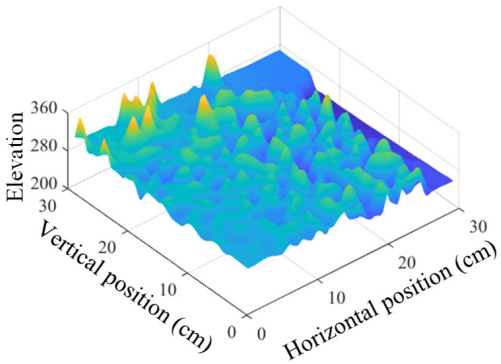


(**d**) AC-10 capacitance imaging

**Figure 9.** *Cont.*

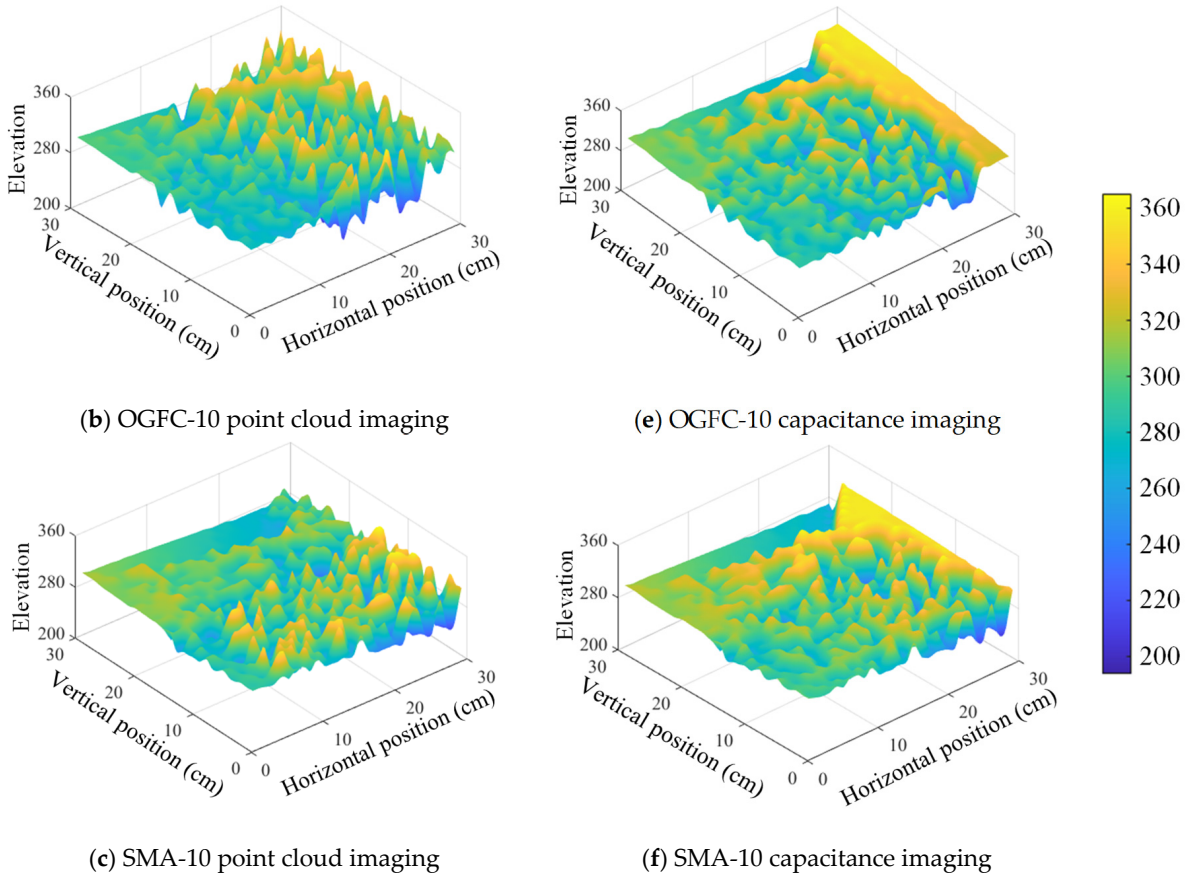


(**b**) OGFC-10 point cloud imaging (**e**) OGFC-10 capacitance imaging

(**c**) SMA-10 point cloud imaging (**f**) SMA-10 capacitance imaging

**Figure 9.** Point cloud and coplanar capacitance imaging of asphalt mixture texture.

**Table 8.** Related macroscopic texture indicators of the asphalt mixture specimens.

| Parameters | AC-10-P | AC-10-C | OGFC-10-P | OGFC-10-C | SMA-10-P | SMA-10-C |
|---|---|---|---|---|---|---|
| MPD (mm) | 0.835 | 0.913 | 2.756 | 2.853 | 2.094 | 2.183 |
| RVD (mm) | 1.925 | 2.054 | 5.782 | 5.983 | 4.548 | 2.674 |
| ETD (mm) | 0.868 | 0.930 | 2.405 | 2.482 | 1.875 | 1.946 |
| MTD (mm) | 0.893 | | 3.324 | | 2.437 | |

**Table 9.** Quantitative comparison of laser scanning and ICCS.

| Parameters | AC-10 | OGFC-10 | SMA-10 |
|---|---|---|---|
| MSE | 0.2734 | 0.2154 | 0.2381 |
| RMSE | 0.5391 | 0.4641 | 0.4906 |
| MAE | 0.3441 | 0.3051 | 0.3208 |
| $R^2$ | 0.7927 | 0.8893 | 0.8255 |
| PCCs | 0.7325 | 0.8528 | 0.8108 |

## 5. Conclusions

In this study, a novel ICCS is designed and optimized for the detection of road texture in asphalt layers. To address the trade-off between signal strength and penetration depth of the ICCS, a comprehensive design and optimization approach is proposed herein. It integrates statistical modeling based on RSM-CCD with the optimization capability of NSGA-II. The fabricated ICCS is applied to detect the surface texture of asphalt mixture specimens with different gradations, and the results are compared with those obtained via laser point-cloud detection. The key findings derived from this research are summarized as follows:

1. The statistical models for signal strength ($C^*$) and penetration depth ($H$) established based on RSM-CCD exhibit excellent consistency with the simulation results, with coefficients of determination ($R^2$) of 0.9561 for $C^*$ and 0.9781 for H, respectively.
2. The ANOVA and 3D response surface plots generated from RSM-CCD are employed to identify the significant variables influencing signal strength ($C^*$) and penetration depth (H). For signal strength, the order of significance (from highest to lowest) is determined as W ≈ L > G; in contrast, the significance ranking for penetration depth is G > L > W. Among the interaction terms, the interaction between W and G is found to be statistically significant.
3. The Pareto optimal solution set is obtained via multi-objective optimization with predefined constraints for optimization objectives, and a simplified multi-attribute decision-making method is adopted to select the final optimal solution. Accordingly, the optimal structural parameters of the ICCS are identified as follows: electrode length (L = 10.02 mm), electrode width (W = 1.50 mm), and inter-finger gap (G = 0.83 mm). The relative error between the simulation results and the predicted values is less than 5%, which validates the reliability of the structural optimization and prediction of the ICCS using the coupled RSM-NSGA-II method.
4. By comparing the height distributions of asphalt mixture specimens with three gradations (OGFC-10, AC-10, and SMA-10) obtained by converting the coplanar capacitance detected by the ICCS with those detected by laser point cloud, the detection results of the ICCS are close to the laser point-cloud data, indicating that it is feasible for road texture detection.

Overall, the findings demonstrate that the proposed method is promising and effective for the multi-objective optimization of the ICCS design. The statistical modeling and multi-objective optimization of the ICCS based on RSM coupled with CCD and NSGA-II provide valuable guidance for engineers and researchers in determining the optimal structural parameters of the ICCS with superior performance. The data collected by the ICCS exhibits obvious two-dimensional matrix characteristics. In the future, deep learning models such as convolutional neural networks and vision transformers can be introduced to perform image-based processing on the capacitance response data, thereby realizing the automatic identification and classification from original signals to texture images, which further improves the detection efficiency and accuracy.

**Author Contributions:** Conceptualization, J.G. and Z.L.; methodology, J.G.; software, J.G.; validation, J.G., B.S. and Z.L.; formal analysis, J.G. and B.S.; investigation, J.G. and B.S.; resources, B.S. and Z.L.; data curation, J.G.; writing—original draft preparation, J.G.; writing—review and editing, B.S. and Z.L.; visualization, J.G.; supervision, Z.L.; project administration, Z.L.; funding acquisition, Z.L. All authors have read and agreed to the published version of the manuscript.

**Funding:** This research received no external funding.

**Data Availability Statement:** The data presented in this study are available from the corresponding author upon reasonable request.

**Conflicts of Interest:** Author Jiejia Guo is employed by Hunan Provincial Communications Planning, Survey & Design Institute Co., Ltd. The remaining authors declare that the research was conducted in the absence of any commercial or financial relationships that could be construed as a potential conflict of interest.

## References


1. Al-Assi, M.; Kassem, E.; Nielsen, R. Using close-range photogrammetry to measure pavement texture characteristics and predict pavement friction. *Transp. Res. Rec.* **2020**, *2674*, 794–805. [CrossRef]
2. Chen, J.; Huang, X.; Zheng, B.; Zhao, R.; Liu, X.; Cao, Q.; Zhu, S. Real-time identification system of asphalt pavement texture based on the close-range photogrammetry. *Constr. Build. Mater.* **2019**, *226*, 910–919. [CrossRef]
3. Cui, X.; Zhou, X.; Lou, J.; Zhang, J.; Ran, M. Measurement method of asphalt pavement mean texture depth based on multi-line laser and binocular vision. *Int. J. Pavement Eng.* **2017**, *18*, 459–471.
4. Dong, S.; Han, S.; Wu, C.; Xu, O.; Kong, H. Asphalt pavement macrotexture reconstruction from monocular image based on deep convolutional neural network. *Comput.-Aided Civ. Infrastruct. Eng.* **2022**, *37*, 1754–1768. [CrossRef]
5. Du, Y.; Weng, Z.; Li, F.; Ablat, G.; Wu, D.; Liu, C. A novel approach for pavement texture characterisation using 2D-wavelet decomposition. *Int. J. Pavement Eng.* **2022**, *23*, 1851–1866.
6. El Gendy, A.; Shalaby, A.; Saleh, M.; Flintsch, G.W. Stereo-vision applications to reconstruct the 3D texture of pavement surface. *Int. J. Pavement Eng.* **2011**, *12*, 263–273. [CrossRef]
7. Gao, L.; Liu, M.; Wang, Z.; Xie, J.; Jia, S. Correction of texture depth of porous asphalt pavement based on CT scanning technique. *Constr. Build. Mater.* **2019**, *200*, 514–520. [CrossRef]
8. Guo, F.; Pei, J.; Zhang, J.; Li, R.; Zhou, B.; Chen, Z. Study on the skid resistance of asphalt pavement: A state-of-the-art review and future prospective. *Constr. Build. Mater.* **2021**, *303*, 124411. [CrossRef]
9. Huang, Y.; Copenhaver, T.; Hempel, P.; Mikhail, M. Development of texture measurement system based on continuous profiles from three-dimensional scanning system. *Transp. Res. Rec.* **2013**, *2367*, 13–22. [CrossRef]
10. Li, Q.; Yang, G.; Wang, K.C.P.; Zhan, Y.; Wang, C. Novel macro- and microtexture indicators for pavement friction by using high-resolution three-dimensional surface data. *Transp. Res. Rec.* **2017**, *2641*, 164–176. [CrossRef]
11. Liang, J.; Gu, X.; Chen, Y.; Ni, F.; Zhang, T. A novel pavement mean texture depth evaluation strategy based on three-dimensional pavement data filtered by a new filtering approach. *Measurement* **2020**, *166*, 108265. [CrossRef]
12. Liu, C.; Li, J.; Gao, J.; Yuan, D.; Gao, Z.; Chen, Z. Three-dimensional texture measurement using deep learning and multi-view pavement images. *Measurement* **2021**, *172*, 108828. [CrossRef]
13. White, G.; Ward, C.; Jamieson, S. Field evaluation of a handheld laser meter for pavement surface macro texture measurement. *Int. J. Pavement Eng.* **2021**, *22*, 950–959.
14. Yang, G.; Wang, K.C.P.; Li, J.Q. Multiresolution analysis of three-dimensional (3D) surface texture for asphalt pavement friction estimation. *Int. J. Pavement Eng.* **2021**, *22*, 1882–1891.
15. Liu, Z.; Yeoh, J.K.W.; Gu, X.; Dong, Q.; Chen, Y.; Wu, W.; Wang, L.; Wang, D. Automatic pixel-level detection of vertical cracks in asphalt pavement based on GPR investigation and improved mask R-CNN. *Autom. Constr.* **2023**, *146*, 104689. [CrossRef]
16. Tong, Z.; Gao, J.; Sha, A.; Hu, L.; Li, S. Convolutional neural network for asphalt pavement surface texture analysis. *Comput.-Aided Civ. Infrastruct. Eng.* **2018**, *33*, 1056–1072. [CrossRef]
17. Weng, Z.; Xiang, H.; Lin, Y.; Liu, C.; Wu, D.; Du, Y. Pavement texture depth estimation using image-based multiscale features. *Autom. Constr.* **2022**, *141*, 104404. [CrossRef]
18. Liu, Z.; Kwan, M.P.; Jiang, W.; Liu, Y.; Cui, B. A Lightweight Multi-Scale Fusion Framework for Traffic Vehicle Detection from Satellite Remote Sensing, UAV, and CCTV Imagery. *IEEE Trans. Geosci. Remote Sens.* **2026**, *67*, 5632717. [CrossRef]
19. Kidner, N.J.; Homrighaus, Z.J.; Mason, T.O.; Garboczi, E.J. Modeling interdigital electrode structures for the dielectric characterization of electroceramic thin films. *Thin Solid Films* **2006**, *496*, 539–545. [CrossRef]
20. Liang, G.; Wang, Y.; Mei, D.; Xi, K.; Chen, Z. A modified analytical model to study the sensing performance of a flexible capacitive tactile sensor array. *J. Micromech. Microeng.* **2015**, *25*, 035017. [CrossRef]
21. Shi, B.; Chen, X.; Hu, X.; Yao, K.; Yan, S.; Dong, Q. Dynamic coplanar array capacitance imaging method for asphalt materials with concealed damages. *IEEE Trans. Intell. Transp. Syst.* **2025**, *26*, 6977–6990. [CrossRef]
22. Shi, B.; Chen, X.; Hu, X.; Yao, K.; Yan, S.; Dong, Q. Internal distress recognition of asphalt materials based on static coplanar array capacitance imaging technology. *IEEE Trans. Intell. Transp. Syst.* **2025**, *26*, 9123–9134. [CrossRef]
23. Zhang, Y.; Zhao, Z.; Yao, X.; Wen, Y.; Luo, X. Planar array capacitive imaging method based on data optimization. *Sens. Actuators A-Phys.* **2022**, *347*, 113941. [CrossRef]
24. Krupa, A.; Lackowski, M.; Jaworek, A. Capacitance sensor for measuring void fraction in small channels. *Measurement* **2021**, *175*, 109046. [CrossRef]
25. Yao, K.; Chen, X.; Dong, Q.; Shi, B.; Hu, X.; Yan, S.; Zhang, J. A novel non-destructive testing approach for asphalt concrete density measurement based on coplanar capacitance: Theory, numerical simulation, and experiment. *Constr. Build. Mater.* **2025**, *458*, 139727. [CrossRef]
26. da Mota, F.R.M.; Pagano, D.J.; Stasiak, M.E. Water volume fraction estimation in two-phase flow based on electrical capacitance tomometry. *IEEE Sens. J.* **2018**, *18*, 6822–6835. [CrossRef]

27. Zhang, J.; Li, R.; Zhang, M.; Peng, J.; Fan, Y.; Ma, S.; Zhang, J. A novel measurement method for ash deposition based on coplanar capacitance principle: Theoretical, numerical and experimental studies. *Energy* **2023**, *282*, 128846. [CrossRef]
28. Zhou, Z.; Wang, R.; Yang, Z.; Shen, X.; Xiong, Y.; Feng, Y. The semi-analytical model of electric field and capacitance in a multilayer-structured interdigital electrode capacitor. *Appl. Math. Model.* **2024**, *136*, 115632. [CrossRef]
29. Igreja, R.; Dias, C.J. Extension to the analytical model of the interdigital electrodes capacitance for a multi-layered structure. *Sens. Actuators A-Phys.* **2011**, *172*, 392–399. [CrossRef]
30. Khan, A.U.; Khan, M.E.; Hasan, M.; Alhazmi, W.; Zakri, W. Analytical evaluation of a coplanar interdigitated sensor capacitance for 1-N-1 multilayered structure. *IEEE Trans. Instrum. Meas.* **2023**, *72*, 9502410. [CrossRef]
31. Dias, C.J.; Igreja, R. A method of recursive images to obtain the potential, the electric field and capacitance in multi-layer interdigitated electrode (IDE) sensors. *Sens. Actuators A-Phys.* **2017**, *256*, 95–106. [CrossRef]
32. Dong, X.; Huang, Q.; Xu, W.; Tang, B.; Yang, S.; Zhu, J.; En, Y. Research on temperature characteristic of parasitic capacitance in MEMS capacitive accelerometer. *Sens. Actuators A-Phys.* **2019**, *285*, 581–587. [CrossRef]
33. Ghione, G.; Goano, M. Revisiting the partial-capacitance approach to the analysis of coplanar transmission lines on multilayered substrates. *IEEE Trans. Microw. Theory Tech.* **2003**, *51*, 2007–2014. [CrossRef]
34. Lee, G.-Y.; Park, J.-H.; Chang, Y.W.; Kang, M.-J.; Cho, S.; Pyun, J.-C. Capacitive biosensor based on vertically paired electrode with controlled parasitic capacitance. *Sens. Actuators B-Chem.* **2018**, *273*, 384–392. [CrossRef]
35. Blume, S.O.P.; Ben-Mrad, R.; Sullivan, P.E. Modelling the capacitance of multi-layer conductor-facing interdigitated electrode structures. *Sens. Actuators B-Chem.* **2015**, *213*, 423–433. [CrossRef]
36. Wang, P.; Guo, B.; Li, N. Multi-index optimization design for electrical resistance tomography sensor. *Measurement* **2013**, *46*, 2845–2853. [CrossRef]
37. Heydarianasl, M.; Rahmat, M.F.a. Design optimization of electrostatic sensor electrodes via MOPSO. *Measurement* **2020**, *152*, 107288. [CrossRef]
38. Liu, Z.; Gu, X.; Kwan, M.P.; Cui, B. Integrated ultrasonic testing and numerical simulation for damage detection in steel bridge deck pavements. *Eng. Struct.* **2026**, *355*, 122421. [CrossRef]
39. Li, Z.; Chen, G.; Li, C.; Fu, J.; Gu, Y.; Li, W.; Yin, X. Performance evaluation of capacitive imaging sensors with different geometries. *Insight* **2018**, *60*, 676–684. [CrossRef]
40. Cao, Z.G.; Wang, Z.C.; Zhao, L.; Fan, F.; Sun, Y. Multi-constraint and multi-objective optimization of free-form reticulated shells using improved optimization algorithm. *Eng. Struct.* **2022**, *250*, 113442. [CrossRef]
41. Cui, B.; Wang, H. Coupled prediction of viscoelastic properties of asphalt mixtures using a multi-task physics-constrained neural network. *Adv. Eng. Inform.* **2026**, *72*, 104437. [CrossRef]
42. Piya, S.; Triki, C.; Al Maimani, A.; Mokhtarzadeh, M. Optimization model for designing personalized tourism packages. *Comput. Ind. Eng.* **2023**, *175*, 108839. [CrossRef]
43. Yi, J.; Xing, L.; Wang, G.; Dong, J.; Vasilakos, A.V.; Alavi, A.H.; Wang, L. Behavior of crossover operators in NSGA-III for large-scale optimization problems. *Inf. Sci.* **2020**, *509*, 470–487. [CrossRef]
44. *JTG E20-2011*; Standard Test Methods of Bitumen and Bituminous Mixtures for Highway Engineering. China Communications Press: Beijing, China, 2011.


**Disclaimer/Publisher's Note:** The statements, opinions and data contained in all publications are solely those of the individual author(s) and contributor(s) and not of MDPI and/or the editor(s). MDPI and/or the editor(s) disclaim responsibility for any injury to people or property resulting from any ideas, methods, instructions or products referred to in the content.